Reticular Synthesis of Porous Molecular 1-Dimensional Nanotubes and 3-Dimensional Networks

A. G. Slater,[1] M. A. Little,[1] A. Pulido,[2] S. Y. Chong,[1] D. Holden,[1] L. Chen,[1] C. Morgan,[1] X. Wu,[1] G. Cheng,[1] R. Clowes,[1] M. E. Briggs,[1] T. Hasell,[1] K. E. Jelfs,[3] G. M. Day[2]* and A. I. Cooper[1]*

[1] Department of Chemistry and Materials Innovation Factory, University of Liverpool, Crown Street, Liverpool L69 7ZD, United Kingdom; [2] School of Chemistry, University of Southampton, Highfield, Southampton SO17 1BJ, United Kingdom; [3] Department of Chemistry, Imperial College London, South Kensington, London SW7 2AZ, United Kingdom.

Synthetic control over pore size and pore connectivity is the crowning achievement for porous metal-organic frameworks. The same level of control has not been achieved for molecular crystals, which are not defined by strong, directional intermolecular coordination bonds. Hence, molecular crystallization is inherently less controllable than framework crystallization, and there are fewer examples of 'reticular synthesis'—where multiple building blocks can be assembled according to a common assembly motif. Here, we apply a chiral recognition strategy to a new family of tubular covalent cages, to create both 1-D porous nanotubes and 3-D diamondoid pillared porous networks. The diamondoid networks are analogous to metal-organic frameworks prepared from tetrahedral metal nodes and linear, ditopic organic linkers. The crystal structures can be rationalized by computational lattice energy searches, which provide an *in silico* screening method to evaluate candidate molecular building blocks. These results are a blueprint for applying the 'node and strut' principles of reticular synthesis to molecular crystals.

Despite many advances in supramolecular chemistry, it is still challenging to control molecular crystallization to create a specific, useful property.[1,2] This is important in the emerging area of porous molecular solids,[3] which have practical advantages such as solution processability. The crystal packing in porous molecular crystals defines the pore dimensions, which in turn define properties

such as guest selectivity.[4,5] The same challenge—control over solid state structure—applies to all functional molecular crystals because crystal packing defines physical properties such as electronic band gap and thermal or electrical conductivity.

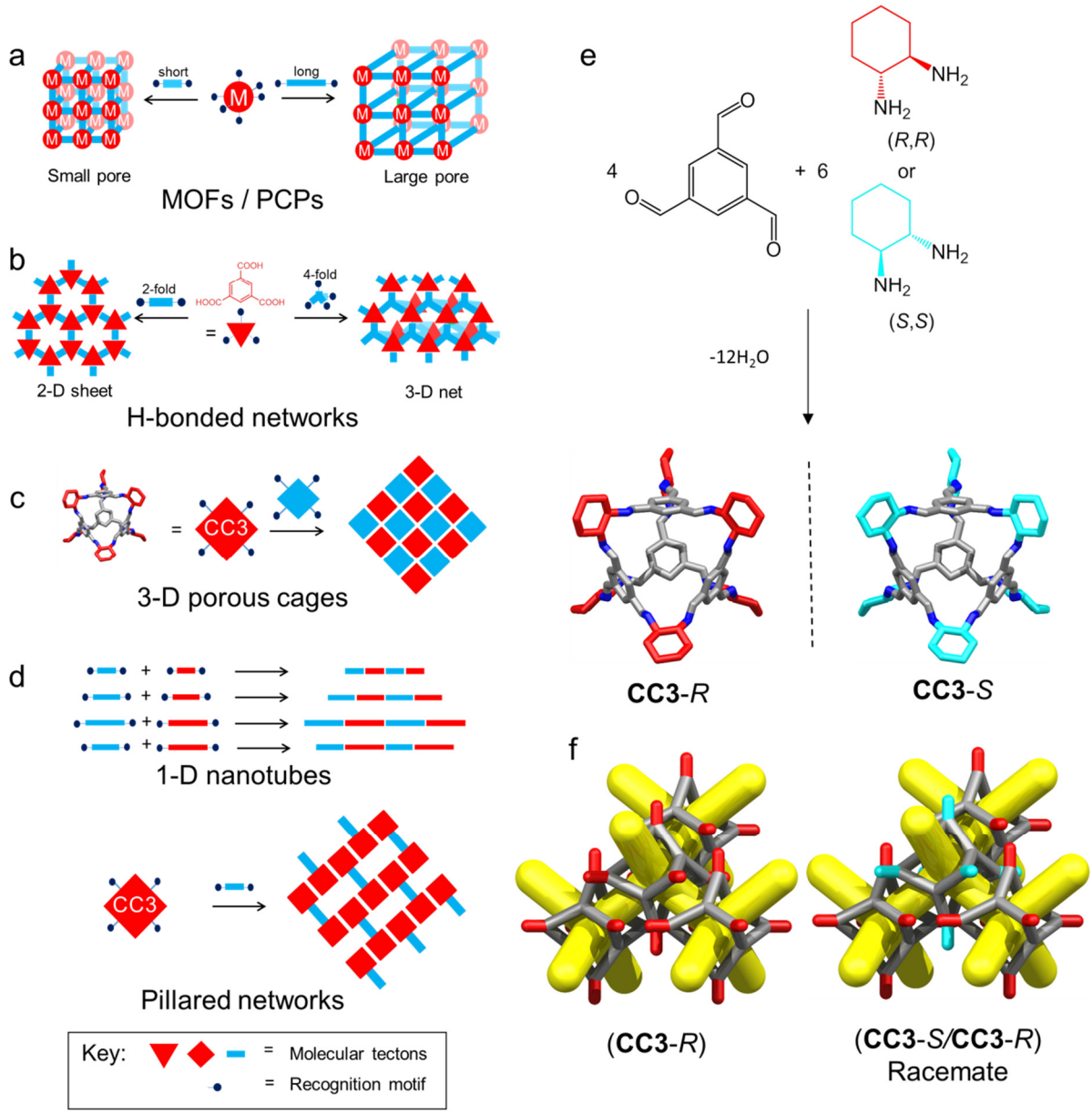

A central paradigm in crystal engineering is to synthesize building blocks, or 'tectons', with strong, directional interactions, such as hydrogen bonding[6] or metal-ligand binding,[7] which direct assembly into a targeted three-dimensional superstructure (**Fig. 1**).[1,2,8,9] For metal-organic frameworks (MOFs) and porous coordination polymers (PCPs), directional metal-ligand bonds are used to do this (**Fig. 1a**).[10-14] Likewise, hydrogen bonding can be used to create organic molecular crystals with defined

network structures (**Fig. 1b**).[9,15,16] We have used chiral recognition to assemble porous organic cages (POCs) into structures with 3-D pore channels (**Fig. 1c**).[3] POCs are rigid molecules with a permanent internal void that is accessible to guests via 'windows' in the cage.[17-19] Control of structure and function for POCs can be difficult, however, because slight changes in the molecular structure[19] or the crystallization solvent[20] can cause a profound change in the crystal packing. Chiral window-to-window interactions (**Fig. 1e,f**) can direct these POCs to assemble into 3-D pore networks in several cases,[19,21,22] but this is not ubiquitous. For example, some cages require specific solvents to template the window-to-window packing.[20]

The chiral cage **CC3**-*S* (**Fig. 1e**) has four windows positioned in a tetrahedral arrangement. Heterochiral window-to-window interactions with the opposite cage enantiomer, **CC3**-*R*, allow the cages to pack more closely than their homochiral equivalents. Previous gas phase density functional theory (DFT) dimer calculations showed that heterochiral dimer pairs were more stable than homochiral dimer pairs (-169 kJ mol^{-1} versus -150 kJ mol^{-1}).[22]

These tetrahedral cages are preconfigured to produce 3-D pore networks (**Fig. 1f**), but 1-D pore channels are also attractive. For example, 1-D pores have been used to study water transport[23,24] and the host-guest chemistry of linear molecules.[25] 1-D porous structures were also used as templates for 1-D nanowires[26] and as efficient molecular sieves.[27] Molecular 1-D nanotubes, a subset of 1-D channel materials, have been reported previously,[30-34] but few are stable to guest removal to yield porous structures.[34,35] Also, molecular self-assembly approaches to form nanotubes have not been demonstrated across a range of different building blocks, as for isoreticular MOFs.

Here, we translate our chiral recognition strategy (**Fig. 1e,f**) to produce 1-D supramolecular nanotubes. Building on this design principle, we use a metal-free equivalent of reticular framework synthesis[10,12,14] to prepare two isoreticular porous pillared structures by heterochiral co-crystallization of tubular (1-D) and tetrahedral (3-D) chiral building blocks. This results in unique materials that are a molecular analogues of extended frameworks composed of tetrahedral metallic nodes and linear, 'ditopic' organic linkers that are able to coordinate two metal separate sites.[10]

Results and discussion

To access new building blocks that might form 1-D pore channels, we first synthesized a series of tetraaldehyde cage precursors with different linker lengths (**Fig. 2a**). Three chiral tubular covalent cages, **TCC1**, **TCC2**, and **TCC3**, were then synthesized from these precursors in [3+6] cycloimination reactions with *R*,*R*- or *S*,*S*-CHDA (**Fig. 1e**; see Supplementary Information, Section 1.3, for detailed experimental methods and synthesis of aldehyde precursors). Unlike our previous family of tetrahedral cages,[19,21,22] these tubular cages comprise of two approximately triangular windows, one at each end of the 'tube', and they can be thought of as linear, ditopic tectons for the assembly of 1-D nanotubes (**Fig. 1d**). Importantly, the cage windows in **TCC1–TCC3** are similar to those in tetrahedral **CC3**, both in size and in shape (**Fig. 2c**), suggesting that they might be used as 'mix and match' recognition motifs for preparing more complex structures (*e.g.*, **Fig. 1d**).

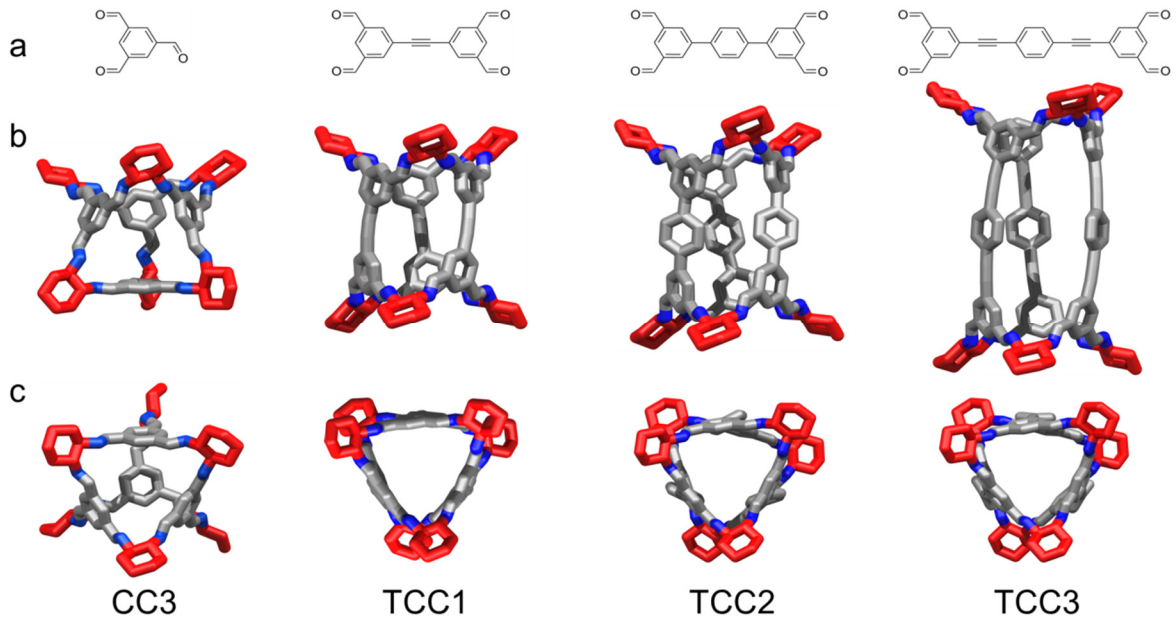

Homochiral tubular cages

We first studied the crystallization of the homochiral -*R* forms of **TCC1–TCC3**. This yielded solvated single crystals of **TCC1**-*R* (space group symmetry $I2_13$) and **TCC2**-*R* ($P3_121$) (**Fig. 3**; see Supplementary Information, Supplementary Table 1, Section 2.1.2, Supplementary Figs 2-7).

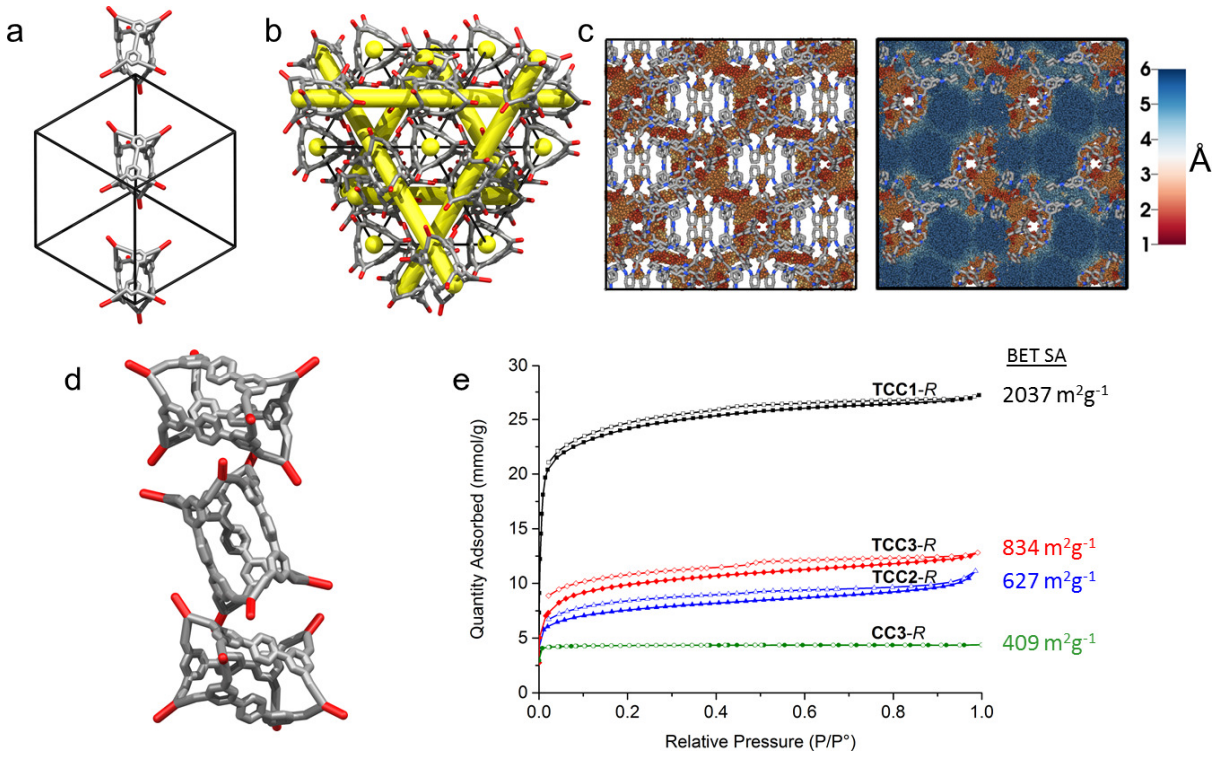

No single crystals of **TCC3**-*R* suitable for single crystal X-ray diffraction (scXRD) could be isolated, but a bulk polycrystalline sample of this material ($P6_3$) was isolated and the cell parameters were deduced from powder X-ray diffraction (PXRD) data (Supplementary Fig. 10).

Although crystalline porous materials were isolated for all three tubular cages, the materials were not isostructural, and each tubular cage packed in a different way (**Fig. 3a,b,d**; see Supplementary Information, 2.1, for crystallographic and gas sorption properties of homochiral TCC cages). Unlike **CC3**-*R* (or **CC3**-*S*, **Fig. 1e,f**), window-to-window packing was not observed between the homochiral TCC cages. We therefore conclude that the homochiral window-to-window interaction is too weak for **TCC1–TCC3** to dominate the crystal lattice energy and hence to drive the formation of supramolecular nanotubes. This may be because the window-to-window interaction propagates in four directions for **CC3** (**Fig. 1f**), and is self-reinforcing, whereas for the hypothetical TCC nanotubes it would propagate along the nanotube only. Nonetheless, even though the homochiral TCC cages do not pack isostructurally, a desolvated material was isolated for **TCC1-*R*** with a high Brunauer-Emmett-Teller (BET) surface area (2037 m^2g^{-1}, **Fig. 3a,b,e**). This is among the highest surface areas

reported for a porous molecular organic solid,[18,35,36] and significantly higher than any of our analogous tetrahedral imine cages.[19,21]

Racemic co-crystals of tubular cages

DFT dimer calculations were performed to establish whether chiral recognition between cages might induce heterochiral window-to-window packing and hence the formation of isostructural nanotubes (Supplementary Information, Section 4.2, Supplementary Table 7). Using **TCC2** as a test case, the heterochiral **TCC2**-*R*/**TCC2**-*S* pair was found to be favoured over the corresponding homochiral **TCC2**-*R* pair (-130 and -104 kJ mol^{-1} respectively), mirroring the heterochiral pairing preference for tetrahedral **CC3**[22,23] (**Fig. 1f**). The stabilization energy of organic molecular co-crystals relative to their single components is typically on the order of a few kJ mol^{-1},[37,38] so that co-crystal formation and structure are sensitive to small chemical changes. The -26 kJ mol^{-1} stabilization predicted by these dimer calculations is on the upper end of the distribution of known co-crystal stabilization energies[37,38] suggesting a robust energetic driving force to co-crystallization of **TCC2**-*R* and **TCC2**-*S*, which might lead to heterochiral window-to-window interactions. When considering the potential heterochiral co-crystallization of **TCC2**-*R* with the tetrahedral cage, **CC3-***S*, a more complex picture emerged due to the weaker binding energy of **TCC2-***R*/**CC3-***S* dimers compared to pure **CC3-***S* dimers. The binding energy of the heterochiral **TCC2**-*R*/**CC3**-*S* dimer was calculated to be *more* stable than a homochiral **TCC2**-*R* dimer (-135 *vs* -104 kJ mol^{-1}), but the heterochiral **TCC2**-*R*/**CC3**-*S* dimer was *less* stable than a homochiral **CC3**-*S* dimer (-135 *vs* -150 kJ mol^{-1}). Ignoring any other possible interactions that do not involve cage windows, these relative energies suggest that a co-crystal of **TCC2**-*R* and **CC3**-*S* is feasible, but that it might contain a mixture of both **CC3**-*S*/**CC3**-*S* and **CC3**-*S*/**TCC2**-*R* interactions to minimize the lattice energy in the solid state.

We next sought to co-crystallize heterochiral mixtures of cages; that is, the three racemates **TCC1**-*R*/**TCC1**-*S*, **TCC2**-*R*/**TCC2**-*S*, **TCC3**-*R*/**TCC3**-*S*, and heterochiral mixtures of **TCC2**-*R*/**TCC3**-*S*, **TCC2**-*R*/**CC3**-*S*, and **TCC1**-*R*/**CC3**-*S*. For the **TCC1**–**TCC3** racemates, equimolar ratios of each cage enantiomer were mixed in solution. In all cases needle-like crystals were obtained

(Supplementary Information, Section 2.2.2, Supplementary Figs. 17–32). These materials, which were all solvates, were characterized by scXRD, and were found to be **TCC1**-*R*/**TCC1**-*S* (space group symmetry $R\bar{3}c$, Et_2O solvate), **TCC2**-*R*/**TCC2**-*S* (space group symmetry *P*6/*mcc*, DCM/IPA solvate; space group symmetry *C*2/*c* and *Cc*, DCM/acetone solvates), and **TCC3**-*R*/**TCC3**-*S* (space group symmetry $R\bar{3}$, DCM/Et_2O solvate). As suggested by the gas phase DFT dimer calculations, all three crystal structures exhibited heterochiral window pairing, thus creating the desired 'isoreticular' 1-D nanotube structures (**Fig. 4**).

Although the 1-D nanotube motif was observed for all three TCC molecules, differences were observed in the crystal packing of the nanotubes. For **TCC1**-*R*/**TCC1**-*S* (**Fig. 4a**) and **TCC3**-*R*/**TCC3**-*S* (space group symmetry $R\bar{3}c$) (**Fig. 4b,c**), the self-assembled nanotubes pack in a pseudohexagonal arrangement with a longitudinal offset to optimize the packing between adjacent nanotubes. The nanotube packing motif is preserved upon desolvation of **TCC1** and **TCC3**, albeit with **TCC3**-*R*/**TCC3**-*S* undergoing a single-crystal-to-single-crystal transformation (Supplementary Information, Section 2.2.3, Supplementary Figs. 33–34). Significant molecular flexibility was observed for the racemate of the longest TCC cage, **TCC3**-*R*/**TCC3**-*S*, whereby the **TCC3** cages 'breathe' upon thermal desolvation and subsequent loading with N_2 (**Fig. 4d–g**).

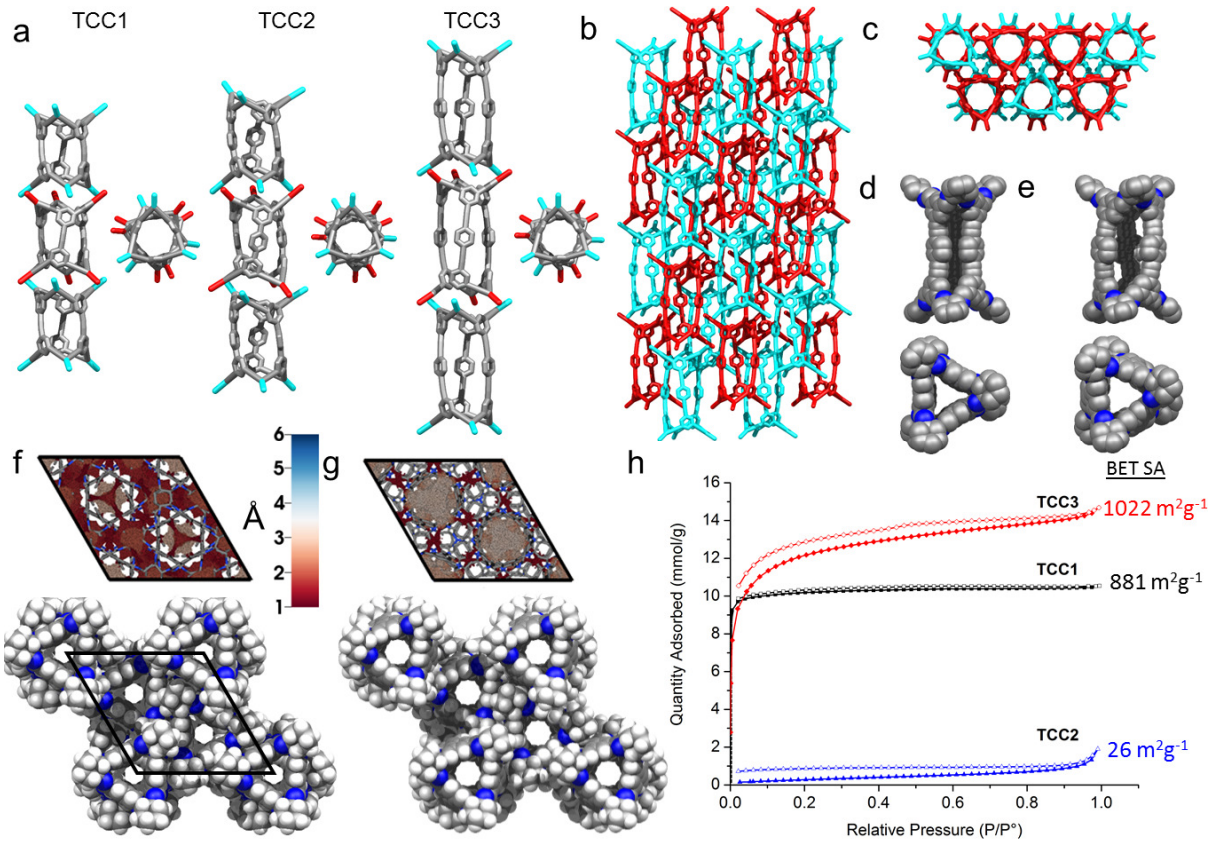

R$\bar{3}$c, *a* = 22.26(4) Å, *c* = 42.35(8) Å R$\bar{3}$c, *a* = 22.420(3) Å, *c* = 42.177(5) Å

Activated bulk crystalline **TCC1-*R*/TCC1-*S*** and **TCC3-*R*/TCC3-*S*** were both found to be microporous with apparent BET surface areas of 881 and 1022 m^2 g^{-1}, respectively. These experimental surface area values correlate well with those predicted from simulations (Supplementary Information, Section 4.4, Supplementary Table 8), and are higher than the surface areas obtained for 3-D tetrahedral cages of comparable dimensions.[19,22] Crystallization of **TCC2-*R*/TCC2-*S*** from DCM/IPA led to a frustrated packing of nanotubes (space group symmetry *P*6/mcc, Supplementary Information, Section 2.2.2.2), whereas crystallization from DCM/acetone gave an efficient, offset packing (two related structures formed with space group symmetry of *C*2/*c* and *Cc* respectively, Supplementary Information, Sections, 2.2.2.3 and 2.2.2.4); that is, racemic nanotubes were formed in both cases, but the crystallization solvent affected the nanotube packing. However, unlike for **TCC1** and **TCC3**, activation of bulk crystalline **TCC2-*R*/TCC2-*S*** gave a poorly crystalline material that was non-porous to nitrogen at 77 K (BET surface area = 26 m^2 g^{-1}; **Fig. 4h**). *In situ* desolvation of a single

crystal of **TCC2**-*R*/**TCC2**-*S* (space group symmetry *Cc*) gave a desolvated crystal structure for **TCC2-*R*/TCC2**-*S* (space group symmetry $R\bar{3}$, Supplementary Fig. 25) where the nanotubes are preserved, but where collapse of the cage occurs. The bulk **TCC2-*R*/TCC2**-*S* material was insufficiently crystalline to determine whether the loss of porosity was due to this cage collapse, to a loss of crystallinity, or to both.

We also calculated the landscapes of possible crystal structures of enantiopure and racemic **TCC1–TCC3** using crystal structure prediction (CSP)[21,39,40,41,42] methods (**Fig. 5**, Supplementary Information, Section 4.6). These are among the most challenging molecules studied to date using CSP methods, and given the size and observed flexibility of the molecules, as well as the influence of solvent inclusion during crystallization, it is beyond the limits of current methods to attempt the *ab initio* prediction of their crystal structures. Instead, our aim was to use these calculations to understand the trends in crystallization behaviour and packing of this series of molecules, in particular with respect to the cage chirality and alignment of cage windows.

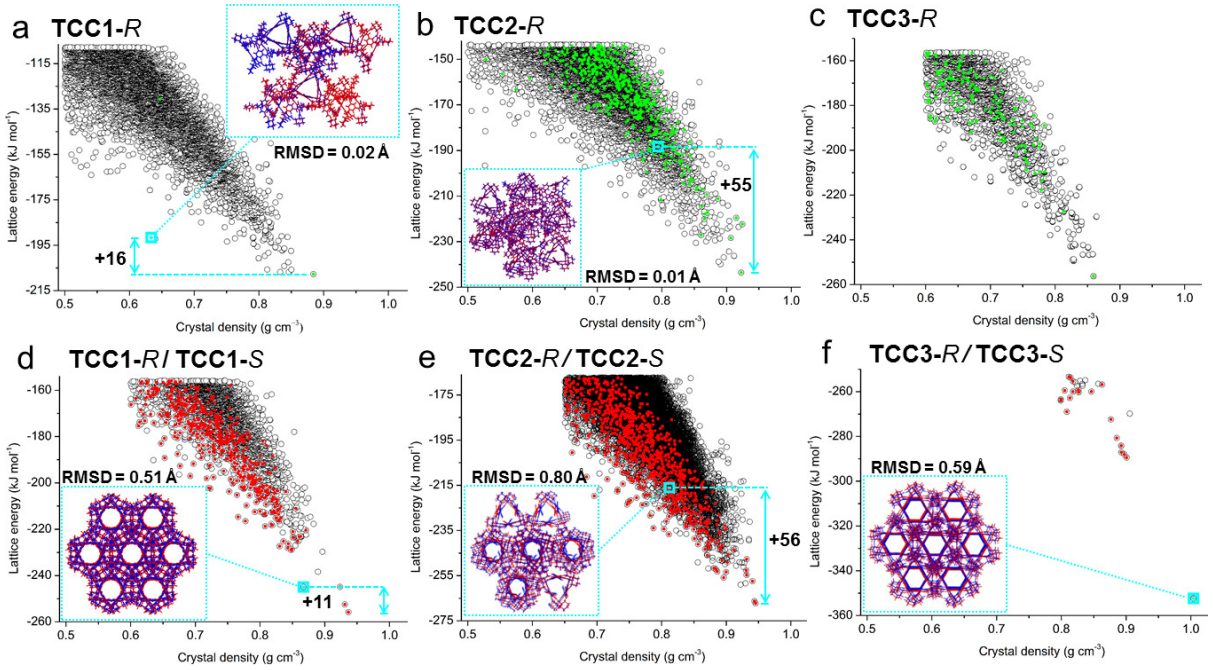

All of the available experimental homochiral and heterochiral crystal packings for **TCC1–TCC3** were found among the predicted structures (**TCC1**-*R*, **TCC2**-*R*, **TCC1**-*R*/**TCC1**-*S*, **TCC2**-*R*/**TCC2**-*S*, and **TCC3**-*R*/**TCC3**-*S*; **Fig. 5**, cyan squares; Supplementary Table 11), although not always as the lowest energy predictions. These calculated landscapes do not include the influence of encapsulated solvent, which can have a significant stabilizing effect[40,41] on the relative stabilities. Hence, it is unsurprising that the solvated **TCC1** and **TCC2** structures are located at higher lattice energies. In particular, the calculations suggest that solvent templating has a significant influence on **TCC2** crystallization: there is a substantial energy gap of 56 kJ mol^{-1} between the experimental solvate for **TCC2**-*R*/**TCC2**-*S* (space group symmetry *Cc;* the highlighted point in **Fig. 5e**) and the lowest energy predicted structure. For the three materials that can be desolvated to yield porous solids, the experimental structures are much closer to the global minimum of their respective landscapes (**TCC1**-*R*; +16 kJ mol^{-1}; **Fig 5a; TCC1**-*R*/**TCC1**-*S*; +11 kJ mol^{-1}; **Fig. 5d**) or at the global minimum energy (**TCC3**-*R*/**TCC3**-*S*; **Fig. 5f**). Hence, these CSP calculations might rationalize the observed instability of **TCC2**-*R*/**TCC2**-*S* to desolvation (*c.f.*, Figs. 5d–f), an insight that is not intuitively obvious from the structures of the cage molecules (**Fig. 2b,c**) or from the gas phase DFT dimer calculations. It has been shown before that stable inclusion structures tend to be located along the low energy edge of crystal structure landscapes, where structures occupy their lowest energy configuration for a given packing

density.[41] Here, we observe that the calculated energy of the highly porous **TCC1**-*R* structure stands out on the landscape (**Fig. 5a**) as unusually stable for such a low density packing mode of this molecule. As we saw previously for the tetrahedral cage, **CC3**,[21] there is a large energy gap (63 kJ mol^{-1}) between the observed minimum energy structure for **TCC3**-*R*/**TCC3**-*S* and the next lowest energy racemic structure. Hence, the crystal packing of the **TCC3** nanotube racemate is predicted correctly (**Fig. 5**) as a result of the strong chiral window-to-window pairing, even when solvent stabilization is ignored.

The preference for racemic crystallization in **TCC1**–**TCC3**, and the importance of heterochiral window-to-window alignment, is made clear by these CSP energy landscapes: the minimum energy racemic structures are more stable than the minimum energy homochiral structure by between 24 and 96 kJ mol^{-1}, depending on the cage (Supplementary Table 11). Window-to-window alignment is rare on the landscapes of the enantiopure **TCC1**-*R*, **TCC2**-*R* and **TCC3**-*R*, being found in fewer than 5 % of predicted structures, and mostly in high energy regions (filled green circles, **Fig. 5a-c**). In contrast, predicted structures that contain heterochiral window-to-window pairs are more dominant on the landscapes of predicted racemates and, in general, occupy the low energy region of the crystal packing landscapes for the three cages (**Fig. 5d–f**, filled red circles). Further analysis of the CSP data, including insights into differences in behaviour across the cage series, can be found in the Supplementary Information (Section 4.6). We have also formed mixed nanotube structures by pairing **TCC2**-*S* with **TCC3**-*R* (*P*3, CH_2Cl_2/1,4-dioxane solvate; Supplementary Figs. 38–39), which supports the generality of a chiral pairing strategy. However, this mixed system is beyond the scope of our CSP methods due to the size and number of molecules in the asymmetric unit.

Racemic co-crystals of tubular and tetrahedral cages

We next looked to extend this chiral pairing strategy to more complex two-component systems by pairing **TCC2**-*R* with the opposite enantiomer of the tetrahedral cage, **CC3**-*S* (**Fig. 1d, Fig. 2b,c**). This is broadly analogous to combining a tetrafunctional, tetrahedral metal-organic secondary building unit with a 'ditopic' organic linker.[10] Co-crystallization of **TCC2**-*R* and **CC3**-*S* in a 1:2 molar ratio from a CH_2Cl_2 solution in the presence of 1,4-dioxane[21] produced a new crystalline phase,

TCC2-*R*·(**CC3**-*S*)$_2$·(1,4-dioxane)$_{17.75}$ (space group $P6_322$, Supplementary Information, Section 2.4, Supplementary Figs. 41–43). Single crystal X-ray diffraction revealed that the structure comprises homochiral, window-to-window **CC3**-*S* layers[41] pillared by heterochiral **CC3**-*S*/**TCC2**-*R* window-to-window interactions (**Fig. 6a**). This material can be compared with stable zeotypic diamond-like topologies, such as the cristobalite-net, and also with the prototypical framework, $Zn(CN)_2$,[10] which comprises tetrahedral nodes (Zn^{2+}) and linear struts (CN^-). In both $Zn(CN)_2$ and our co-crystal, "adamantane units"[10] dominate the structure (see yellow channels; **Fig. 6a**), but unlike $Zn(CN)_2$, the **TCC2**-*R*·(**CC3**-*S*)$_2$·co-crystal does not interpenetrate. Also, this molecular crystal has a 2:1 ratio of tetrahedral to linear building blocks, rather than the 1:2 ratio in $Zn(CN)_2$, because of the formation of the **CC3**-*S* layers (**Fig. 6a**). This can be rationalized by the calculated relative energies for **TCC2/CC3** dimers and pure **CC3** dimers, discussed above. These relative energies cause all of the **TCC2**-*R* cage 'pillars' to form heterochiral window interactions with **CC**3-*S*, while three out of four windows in **CC**3-*S* pair homochirally. Hence, the loss of one favourable **CC3**-*S*/**CC3**-*S* pair per cage is compensated by the formation of an even more favourable **CC3**-*S*/**TCC2**-*R* interaction (*i.e.*, by DFT, a **CC3**-*S*/**TCC2**-*R* dimer gains 31 kJ mol^{-1} with respect to a **TCC2**-*R* dimer, while losing one **CC3**-*S* dimer costs only 15 kJ mol^{-1}; Supplementary Table 7). Despite this difference in the assembly mode, both **TCC2**-*R*·(**CC3**-*S*)$_2$ and $Zn(CN)_2$[10] can be considered to be diamondoid structures as a result of the connectivity in the **CC3**-*S* layers, although for the co-crystal there is an elongation along the axis of the **TCC2**-*R* struts. Our approach can also be extended to other ditopic cage linkers, much as for isoreticular MOFs. For example, the cage pair **CC3**-*S*/**TCC1**-*R* crystallises as **TCC1**-*R*·(**CC3**-*S*)$_2$ (space group $P6_322$, CH_2Cl_2/Et_2O solvate, Supplementary Figs. 45–46), which is isoreticular to the **TCC2**-*R*·(**CC3**-*S*)$_2$ co-crystal (**Figure 6d**). The interlayer spacing between the **CC3**-*S* layers in **TCC1**-*R*·(**CC3**-*S*)$_2$ is approximately 1.4 Å shorter than in **TCC2**-*R*·(**CC3**-*S*)$_2$, in keeping with the expected shortening due to replacing an aromatic ring with an acetylene bond in the **TCC1** cage (approximately1.6 Å).

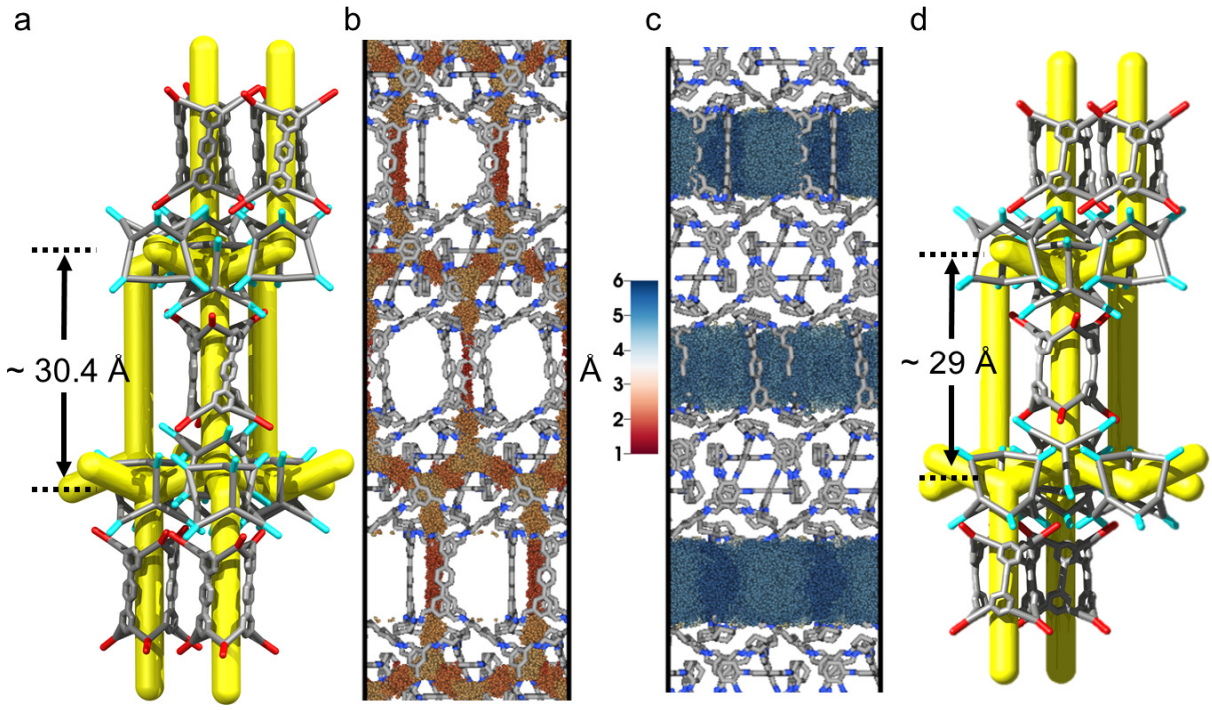
a
b
c
d
~ 30.4 Å
~ 29 Å
Å
6
5
4
3
2
1

Both **TCC2**-*R*·(**CC3**-*S*)$_2$ and its 'isoreticular' analogue, **TCC1**-*R*·(**CC3**-*S*)$_2$, are stable after thermal desolvation of the pores (Supplementary Information, Section 2.5, Supplementary Fig. 47). The 3-D pore structure of the **TCC2**-*R*·(**CC3**-*S*)$_2$ co-crystal features two distinct pore networks: one that runs through the intrinsic cage cavities (**Fig. 6b**), and a larger one that passes though the extrinsic voids between the **TCC2**-*R* pillars and the **CC3**-*S* layers (**Fig. 6c**). Gas uptakes for this co-crystal correlate well with those predicted from the single crystal structure (Supplementary Table 8), and the material was found to have a high BET surface area of 1363 $m^2 g^{-1}$ (Supplementary Fig. 44). Hence, the co-crystal is more porous than either of the individual co-formers (**CC3**-*R*: 409–624 $m^2 g^{-1}$;[19,22] **TCC2**-*R*: 627 $m^2 g^{-1}$). These two co-crystals suggest a more general 'mix-and-match' strategy that is analogous to changing linkers in isoreticular MOFs.

Conclusions

Chiral recognition has been used to engineer the crystal packing of a new series of porous organic cages to yield supramolecular nanotubes from ditopic molecules in a targeted way. Building on this principle, we prepared two pillared co-crystals from ditopic linkers and tetrahedral nodes via molecular reticular synthesis. Gas phase DFT dimer calculations and crystal structure prediction calculations rationalize the structures that are formed and provide a design strategy for future materials. This 'mix and match' cage pairing strategy parallels isorecticular MOFs and PCPs, where organic linkers are paired with metallic secondary building units, but with some unique differences — for example, in all cases, the cages are solution processable. More generally, the ability to position organic molecules in a controllable manner in the solid state opens up possibilities for the design of new function in multiple applications such as optoelectronics,[44,45] superconductors,[46,47] organic magnets,[48] and organic photocatalysts.[49]

Methods

Synthesis of TCC series typified by TCC2-*R*. To a stirred suspension of 3,3''',5,5'''-tetraformyl-1,1':4',1'''-terphenyl (2.0 g, 5.84 mmol) and TFA (5 drops) in DCM (20 mL) was added a solution of *R*,*R*-cyclohexanediamine (1.34 g, 11.7 mmol) in DCM (28 mL). The mixture was stirred overnight at room temperature, during which time the solution turned yellow and the tetraaldehyde compound was observed to dissolve. After 5 days, the reaction mixture was diluted with DCM and the mixture was filtered. The filtrate was concentrated to ~20 mL, hexane (40 mL) was charged with stirring and the resulting white precipitate was collected via suction filtration to yield pure product (2.54 g, 87 %) ^{1}H NMR (400 MHz, $CDCl_3$, δ (ppm)): 8.27 (s, 6 H), 8.17 (s, 6 H), 7.85 (m, 12 H), 7.41 (s, 6 H), 7.07 (s, 12 H), 3.46 (br. s., 6 H), 3.21 (d, *J* = 6.5 Hz, 6 H), 2.12 - 1.99 (m, 6 H), 1.91 (d, *J* = 8.0 Hz, 12 H), 1.82 (br. s., 6 H), 1.65 (br. s., 12 H), 1.54 (d, *J* = 8.6 Hz, 12 H). ^{13}C NMR (101 MHz, $CDCl_3$, δ (ppm)): 161.4, 160.8, 141.1, 139.4, 137.0, 136.2, 131.5, 127.3, 125.7, 75.5, 74.1, 32.6, 32.0, 24.5, 24.5. MS(MALDI-TOF)$^{+}$: calcd for $C_{102}H_{103}N_{12}$ $[M+H]^{+}$: 1494.8350; found: 1496. MS(ESI, **TCC2**-*R*)$^{+}$: calcd for $C_{102}H_{103}N_{12}$ $[M+H]^{+}$: 1495.8429; found: 748.4320 $[M+2H]^{2+}$, 499.2942 $[M+3H]^{3+}$; MS (ESI, **TCC2**-*S*)$^{+}$: calcd for $C_{102}H_{103}N_{12}$ $[M+H]^{+}$: 1495.8429; found: 748.4302 $[M+2H]^{2+}$, 499.2932 $[M+3H]^{3+}$. **TCC1**-*R*, **TCC1**-*S*, **TCC2**-*S*, **TCC3**-*R*, and **TCC3**-*S* were all prepared using this method and the appropriate starting materials.

Density functional theory (DFT) calculations for isolated cage pairs. DFT calculations were performed in the mixed Gaussian and plane waves program CP2K/QUICKSTEP.[50, 51] Isolated cage molecules were taken from the single crystal X-ray diffraction structures and then arranged by hand to form **CC3**-*R*/**TCC2**-*R*, **CC3**-*R*/**TCC2**-*S*, **TCC2**-*R*/**TCC2**-*R* and **TCC2**-*R*/**TCC2**-*S* pairings. Several starting configurations were considered to ensure the lowest energy packing mode was found. These were also cross-checked against the single crystal X-ray diffraction structures when available. The PBE functional[52] with the molecularly optimised TZVP-MOLOPT basis set[53] was used with the GTH-type pseudopotential,[54] a plane wave grid cutoff of 350 Ry and the Grimme-D3 dispersion

correction.[55] Once the cage pairs were fully optimised, the binding energy between the cages was then calculated as:

$$E_{\text{binding energy}} = E_{\text{pair}} - E_{\text{cage I}} - E_{\text{cage II}} \qquad (1)$$

Where $E_{\text{cage I}}$ and $E_{\text{cage II}}$ are the energies of the geometry optimised single cages.

Visual pore size distribution (vPSD) plots. The vPSD plots of the five systems were generated using Zeo++. A small probe radius of 1.0 Å was used to highlight the accessible pore regions over a sampling of 1,000,000 points. This was then visualised in VisIt package,[56] using a consistent colouring range of 1.0–6.0 Å. To highlight any larger pore channels and cavities for each structure, the small probe radii were removed from the raw data, and the figures re-plotted. The size of the probes removed was system dependant, and the values are shown in Supplementary Table 10.

Crystal structure prediction. Crystal structure prediction was performed using quasi-random structure generation using the Global Lattice Energy Explorer software,[39] followed by lattice energy minimisation using an atom-atom intermolecular force field with empirically parameterised repulsion-dispersion interactions and an atomic multipole electrostatic model. All lattice energy minimisations were performed using the crystal structure modelling software DMACRYS.[57] Molecular geometries were held rigid through all stages of the calculations, at geometries of the isolated molecules, calculated using DFT (M06-2X/6-311G**). Crystal structures of the enantiomerically pure (-*R*) systems were generated in 14 chiral space groups and in 13 non-chiral space groups for the racemic structures, all assuming one molecule in the asymmetric unit of the crystal structure (Z`=1). 10,000 trial crystal structures were generated and lattice energy minimised for each molecule in each space group. Duplicate crystal structures were identified and removed after lattice energy minimisation using the COMPACK algorithm, which was also used to search for packing motifs within the predicted structures.[58] All CSP datasets supporting this study are openly available from the University of Southampton repository at http://dx.doi.org/10.5258/SOTON/399193.

Crystallographic details. All single crystal structures were refined by full-matrix least squares on $|F|^2$ by SHELXL.[59] Supplementary CIF's, that include structure factors, have been deposited with the

Cambridge Crystallographic Data Centre (CCDC) as deposition numbers CCDC 1453923, **TCC1**-*R*·10.75(MeOH)·12.64(H_2O); CCDC 1453927, **TCC2**-*R*·9.5(MeOH)·6.25(H_2O); CCDC 1453928, **TCC2**-*R*·4.33(NMP)·4(MeOH); CCDC 1453929, **TCC2**-*R*·1.76(NMP); CCDC 1453924, **TCC1**·5(Et_2O); CCDC 1453932, **TCC2**·5.5(CH_2Cl_2)·5.5(IPA); CCDC 1453930, **TCC2**·3(CH_2Cl_2)·3.5(C_3H_6O); CCDC 1453931, **TCC2**·2.88(CH_2Cl_2)·3.46(C_3H_6O)·3.25(H_2O); CCDC 1453934, **TCC2**; CCDC 1453933, **TCC2**·0.44(H_2O); CCDC 1453936, 2(**TCC3**)·5.75(Et_2O)·13(H_2O); CCDC 1453939, **TCC3**·2.5(H_2O); CCDC 1453937, **TCC3**; CCDC 1453938, **TCC3**·13(N_2); CCDC 1453935, **TCC2**-*S*·**TCC3**-*R*·17(CH_2Cl_2)·17($C_4H_8O_2$); CCDC 1453926, **TCC2**-*R*·2(**CC3**-*S*)·13($C_4H_8O_2$)·8(CH_2Cl_2); CCDC 1453925, **TCC2**-*R*·2(**CC3**-*S*); CCDC 1491074, **TCC1**-*R*·2(**CC3**-*S*)·10.65($C_4H_{10}O$)·10.65(CH_2Cl_2); CCDC 1491073, **TCC1**-*R*·2(**CC3**-*S*). These data files can be obtained free of charge *via* http://www.ccdc.cam.ac.uk/data_request/cif. Full synthetic, characterisation, crystallographic, and computational details are available in the Supplementary Information.

Acknowledgements:

We acknowledge funding from the EPSRC (grants EP/J01110X/1 and EP/K018132/1) and the European Research Council under the European Union's Seventh Framework Programme (FP/2007-2013)/ERC through grant agreements n. 307358 (ERC-stG-2012-ANGLE) and n. 321156 (ERC-AG-PE5-ROBOT). KEJ and TH thank the Royal Society for University Research Fellowships. We thank Diamond Light Source for access to beamlines I19 (MT8728, and MT11231) and I11 (EE12336) that contributed to the results presented here, and thank Mark Warren, and Sarah Barnett for their assistance. We thank the Advanced Light Source, supported by the Director, Office of Science, Office of Basic Energy Sciences, of the U.S. Department of Energy under Contract No. DE-AC02-05CH11231, and thank Simon J. Teat, and Kevin J. Gagnon for their assistance. We acknowledge the ARCHER UK National Supercomputing Service via UK's HPC Materials Chemistry Consortium membership, which is funded by EPSRC (EP/L000202), as

well as the use of the IRIDIS High Performance Computing Facility, and associated support services at the University of Southampton, in the completion of this work. We thank Mike Jones and the Centre for Materials Discovery for assistance with LC-MS measurements, and David McMahon for assistance with powder pattern similarity calculations.

Author contributions: A.G.S. and A.I.C conceived the project. A.G.S., M.E.B., X.W., G.C., and C.M. prepared the precursors and cage molecules. A.G.S., C.M., and M.A.L. crystallized and co-crystallized the cage molecules. M.A.L. and S.Y.C. interpreted the X-ray data. R.C., T.H., and L.C. interpreted the sorption data. A.P. and G.M.D. carried out and interpreted the crystal structure prediction calculations. K.E.J. modelled the cage conformers and carried out and interpreted gas phase dimer calculations. D.H. constructed and interpreted the variable pore size distribution models. All authors interpreted the structures and contributed to the preparation of the manuscript.

Competing financial interests: The authors declare no competing financial interests.

References

1 Moulton, B. & Zaworotko, M. J. From molecules to crystal engineering: supramolecular isomerism and polymorphism in network solids. *Chem. Rev.,* **101**, 1629-1658 (2001).

2 Desiraju, G. R. Crystal engineering: from molecule to crystal. *J. Am. Chem. Soc.* **135**, 9952-9967 (2013).

3 Mastalerz, M. Shape-persistent organic cage compounds by dynamic covalent bond formation. *Angew. Chem. Int. Ed.* **49**, 5042-5053 (2010).

4 Chen, L. *et al.* Separation of rare gases and chiral molecules by selective binding in porous organic cages. *Nature Mater.* **13**, 954-960 (2014).

5 Slater, A. G. & Cooper, A. I. Function-led design of new porous materials. *Science* **348**, aaa8075 (2015).

6 Desiraju, G. R. Hydrogen bridges in crystal engineering: interactions without borders. *Acc. Chem. Res.* **35**, 565-573 (2002).

7 Blake, A. J. *et al.* Inorganic crystal engineering using self-assembly of tailored building-blocks. *Coord. Chem. Rev.* **183**, 117-138 (1999).

8 Kitagawa, S., Kitaura, R. & Noro, S. Functional porous coordination polymers. *Angew. Chem. Int. Ed.* **43,** 2334-2375 (2004).

9 Simard, M., Su, D. & Wuest, J. D. Use of hydrogen-bonds to control molecular aggregation - self-assembly of 3-dimensional networks with large chambers. *J. Am. Chem. Soc.* **113**, 4696-98 (1991).

10 Hoskins, B. F. & Robson, R. Design and construction of a new class of scaffolding-like materials comprising infinite polymeric frameworks of 3-D-linked molecular rods. A reappraisal of the $Zn(CN)_2$ and $Cd(CN)_2$ structures and the synthesis and structure of the diamond-related frameworks $[N(CH_3)_4][Cu^{I}Zn^{II}(CN)_4]$ and Cu^{I}[4,4′,4″,4‴-tetracyanotetraphenylmethane]$BF_4.xC_6H_5NO_2$. *J .Am. Chem. Soc.* **112,** 1546-1554 (1990).

11 Kondo, M., Yoshitomi, T., Seki, K., Matsuzaka, H. & Kitagawa, S. Three-dimensional framework with channeling cavities for small molecules: $\{[M_2(4,4'\text{-bpy})_3(NO_3)_4]\cdot xH_2O\}_n$ (M = Co, Ni, Zn). *Angew. Chem. Int. Ed.* **36**, 1725-1727 (1997).

12 Eddaoudi, M. *et al.* Systematic design of pore size and functionality in isoreticular MOFs and their application in methane storage. *Science* **295**, 469-472 (2002).

13 Férey, G. *et al.* A chromium terephthalate-based solid with unusually large pore volumes and surface area. *Science* **309**, 2040-2042 (2005).

14 Furukawa, H., Cordova, K. E., O'Keeffe, M. & Yaghi, O. M. The chemistry and applications of metal-organic frameworks. *Science* **341**, 974 (2013).

15 Ducharme, Y. & Wuest, J. D. Use of hydrogen-bonds to control molecular aggregation - extensive, self-complementary arrays of donors and acceptors. *J. Org. Chem.* **53**, 5787-5789 (1988).

16 Zerkowski, J. A., Seto, C. T. & Whitesides, G. M. Solid-state structures of rosette and crinkled tape motifs derived from the cyanuric acid melamine lattice. *J. Am. Chem. Soc.* **114**, 5473-5475 (1992).

17 Mitra, T. *et al.* Molecular shape sorting using molecular organic cages. *Nat. Chem.* **5**, 276-281 (2013).

18 Zhang, G., Presly, O., White, F., Oppel, I. M. & Mastalerz, M. A permanent mesoporous organic cage with an exceptionally high surface area. *Angew. Chem. Int. Ed.* **53**, 1516-1520, (2014).

19 Tozawa, T. *et al.* Porous organic cages. *Nat. Mater.* **8**, 973-978 (2009).

20 Hasell, T. *et al.* Controlling the crystallization of porous organic cages: molecular analogs of isoreticular frameworks using shape-specific directing solvents. *J .Am. Chem. Soc.* **136**, 1438-1448 (2014).

21 Jones, J. T. A. *et al.* Modular and predictable assembly of porous organic molecular crystals. *Nature* **474**, 367-371 (2011).

22 Hasell, T., Chong, S. Y., Jelfs, K. E., Adams, D. J. & Cooper, A. I. Porous organic cage nanocrystals by solution mixing. *J. Am. Chem. Soc.* **134**, 588-598 (2012).

23 Unruh, D. K., Gojdas, K., Libo, A. & Forbes, T. Z. Development of metal-organic nanotubes exhibiting low-temperature, reversible exchange of confined "ice channels". *J . Am. Chem. Soc.* **135**, 7398-7401 (2013).

24 Hummer, G., Rasaiah, J. C. & Noworyta, J. P. Water conduction through the hydrophobic channel of a carbon nanotube. *Nature* **414**, 188-190 (2001).

25 Ronson, T. K., Zarra, S., Black, S. P. & Nitschke, J. R. Metal-organic container molecules through subcomponent self-assembly. *Chem. Commun.* **49**, 2476-2490 (2013).

26 Xia, Y. N. *et al.* One-dimensional nanostructures: synthesis, characterization, and applications. *Adv. Mater.* **15**, 353-389 (2003).

27 Herm, Z. R. *et al.* Separation of hexane isomers in a metal-organic framework with triangular channels. *Science* **340**, 960-964 (2013).

28 He, L. *et al.* Shape-persistent macrocyclic aromatic tetrasulfonamides: molecules with nanosized cavities and their nanotubular assemblies in solid state. *Proc. Natl. Acad. Sci. USA* **103**, 10850-10855 (2006).

29 Liu, Z. *et al.* Assembly of supramolecular nanotubes from molecular triangles and 1,2-dihalohydrocarbons. *J. Am. Chem. Soc.* **136**, 16651-16660 (2014).

30 Ghadiri, M. R., Granja, J. R., Milligan, R. A., Mcree, D. E. & Khazanovich, N. Self-assembling organic nanotubes based on a cyclic peptide architecture. *Nature* **366**, 324-327 (1993).

31 Wu, X. B. *et al.* Robust ordered bundles of porous helical nanotubes assembled from fully rigid ionic benzene-1,3,5-tricarboxamides. *Chem.-Eur. J.* **21**, 15388-15394 (2015).

32 Hong, B. H. *et al.* Self-assembled arrays of organic nanotubes with infinitely long one-dimensional H-bond chains. *J. Am. Chem. Soc.* **123**, 10748-10749 (2001).

33 Frischmann, P. D., Sahli, B. J., Guieu, S., Patrick, B. O. & MacLachlan, M. J. Sterically-limited self-assembly of Pt4 macrocycles into discrete non-covalent nanotubes: porous supramolecular tetramers and hexamers. *Chem.-Eur. J.* **18**, 13712-13721 (2012).

34 Ji, Q. *et al.* Cyclotetrabenzoin: facile synthesis of a shape-persistent molecular square and its assembly into hydrogen-bonded nanotubes. *Chem.-Eur. J.* **21**, 17205-17209 (2015).

35 Schneider, M. W. *et al.* Periphery-substituted [4+6] salicylbisimine cage compounds with exceptionally high surface areas: influence of the molecular structure on nitrogen sorption properties. *Chem.-Eur. J.* **18**, 836-847 (2012).

36 Mastalerz, M. & Oppel, I. M. Rational construction of an extrinsic porous molecular crystal with an extraordinary high specific surface area. *Angew. Chem. Int. Ed.* **51**, 5252-5255, (2012).

37 Issa, N., Karamertzanis, P. G., Welch, G. W. A. and Price, S. L. Can the formation of pharmaceutical cocrystals be computationally predicted? *Crys. Growth Des.* **9**, 442-453, (2009).

38 Chan, H. C. S., Kendrick, J., Neumann, M. A. and Leusen, F. J. J. Towards *ab initio* screening of co-crystal formation through lattice energy calculations and crystal structure prediction of nicotinamide, isonicotinamide, picolinamide and paracetamol multi-component crystals. *CrystEngComm.* **15**, 3799-3807, (2013).

39 Case, D. H., Campbell, J. E., Bygrave, P. J. and Day, G. M. Convergence properties of crystal structure prediction by quasi-random sampling. *J. Chem. Theory Comput.* **12**, 910-924 (2016).

40 Pyzer-Knapp, E. O. *et al.* Predicted crystal energy landscapes of porous organic cages. *Chem. Sci.* **5**, 2235-2245 (2014).

41 Cruz-Cabeza, A. J., Day, G. M. & Jones, W. Predicting inclusion behaviour and framework structures in organic crystals. *Chem.-Eur. J.* **15**, 13033-13040 (2009).

42 Rodriguez-Albelo, L. M., *et al.* Zeolitic polyoxometalate-based metal-organic frameworks (Z-POMOFs): Computational evaluation of hypothetical polymorphs and the successful targeted synthesis of the redox-active Z-POMOF1. *J. Am. Chem. Soc.* **131**, 16078-16087.

43 Little, M. A. *et al.* Trapping virtual pores by crystal retro-engineering. *Nat. Chem.* **7**, 153-159 (2015).

44 Marder, S. R., Kippelen, B., Jen, A. K. Y. & Peyghambarian, N. Design and synthesis of chromophores and polymers for electro-optic and photorefractive applications. *Nature* **388**, 845-851 (1997).

45 Dou, J. H. *et al.* Fine-tuning of crystal packing and charge transport properties of BDOPV derivatives through fluorine substitution. *J. Am. Chem. Soc.* **137**, 15947-15956 (2015).

46 Haddon, R. C. Design of organic metals and superconductors. *Nature* **256**, 394-396 (1975).

47 Coronado, E., Galan-Mascaros, J. R., Gomez-Garcia, C. J. & Laukhin, V. Coexistence of ferromagnetism and metallic conductivity in a molecule-based layered compound. *Nature* **408**, 447-449 (2000).

48 Crayston, J. A., Devine, J. N. & Walton, J. C. Conceptual and synthetic strategies for the preparation of organic magnets. *Tetrahedron* **56**, 7829-7857 (2000).

49 Weingarten, A. S. *et al.* Supramolecular packing controls H_2 photocatalysis in chromophore amphiphile hydrogels. *J. Am. Chem. Soc.* **137**, 15241-15246 (2015).

50 VandeVondele, J. *et al.* QUICKSTEP: Fast and accurate density functional calculations using a mixed Gaussian and plane waves approach. *Comput. Phys. Commun.* **167,** 103-128 (2005).

51 The CP2K developers group: http://cp2k.berlios.de

52 Perdew, J. P., Burke, K. & Ernzerhof, M. Generalized gradient approximation made simple. *Phys. Rev. Lett.* **77**, 3865-3868 (1996).

53 VandeVondele, J. & Hutter, J. Gaussian basis sets for accurate calculations on molecular systems in gas and condensed phases. *J. Chem. Phys.* **127** (2007).

54 Goedecker, S., Teter, M. & Hutter, J. Separable dual-space Gaussian pseudopotentials. *Phys. Rev. B.* **54**, 1703-1710 (1996).

55 Grimme, S., Antony, J., Ehrlich, S. & Krieg, H. A consistent and accurate ab initio parametrization of density functional dispersion correction (DFT-D) for the 94 elements H-Pu. *J. Chem. Phys.* **132** (2010).

56 Childs, H. *et al. VisIt: An End-User Tool for Visualizing and Analyzing Very Large Data*, <https://wci.llnl.gov/simulation/computer-codes/visit> (2012).

57 Price, S. L. *et al.* Modelling organic crystal structures using distributed multipole and polarizability-based model intermolecular potentials. *Phys. Chem. Chem. Phys.* **12,** 8478-8490 (2010).

58 Chisholm, J. & Motherwell, S. COMPACK: a program for identifying crystal structure similarity using distances. *J. of App. Cryst.* **38,** 228-231 (2005).

59 Sheldrick, G. Crystal structure refinement with SHELXL. Acta Cryst. Sect. C 71, 3-8 (2015).

Figure captions.

Figure 1. Reticular synthesis of extended frameworks and molecular crystals. a) Isoreticular metal-organic frameworks (MOFs) / porous coordination polymers (PCPs); b) hydrogen-bonded networks; c) 3-D porous organic cages, using chiral window-to-window recognition; d) 1-D isoreticular molecular nanotubes and porous pillared molecular networks (this work). e) Synthesis of porous tetrahedral cages **CC3**-*R* and **CC3**-*S* from triformylbenzene (TFB) and cyclohexanediamine (CHDA). For **CC3**-*R*, the cyclohexane groups are shown in red; for **CC3**-*S*, in turquoise; other C, grey; N, blue; H omitted. f) Schematic representation of the desolvated homochiral **CC3**-*R* and racemic (**CC3**-*R*/**CC3**-*S*) crystal structures, pore network shown in yellow, simplified cage frame in grey, simplified cyclohexyl vertices in red (-*R*) and turquoise (-*S*).

Figure 2. **Chiral, tubular covalent cage as linear, ditopic building blocks.** a) Linear tetraaldehyde precursors for the TCC series plus the 1,3,5-triformylbenzene precursor for **CC3** (left); b) side-view and c) view through the cage windows of the tetrahedral cage **CC3** and the trigonal prismatic cage family, **TCC1**–**TCC3**, obtained from single crystal X-ray structures; -*R* cage enantiomers are shown. Hydrogen atoms and solvent removed for clarity, colours are as in **Fig. 1e**.

Figure 3. Crystal structures for non-isoreticular homochiral TCC1-*R* **and TCC2**-*R* **and gas sorption isotherms for TCC1**-*R*, **TCC2**-*R*, and **TCC3**-*R*. Solvent molecules and H atoms removed for clarity, simplified cyclohexyl vertices in red, other C, grey. (a) Crisscross crystal packing diagram of adjacent **TCC1**-*R* molecules from the solvated single crystal structure of **TCC1**-*R*. Although the **TCC1**-*R* molecules are aligned, they are separated in the lattice and there are no window-to-window interactions between cages; (b) crystal packing in solvated **TCC1**-*R*, pore network shown in yellow; again, while pores run through the cage windows, these windows do not interact with each other; (c) pore size visualizations for the **TCC1**-*R* structure showing one smaller interconnected pore network (left) running through the cages themselves (probe radii from 1.0 to 3.0 Å; *c.f.*, yellow channels in (b)), interconnected with a larger pore network, shown in blue (right, probe radii from 1.0 to 6.0 Å), running between the cages to give a hierarchically porous structure; (d) offset crystal packing of

TCC2-*R* molecules in solvated **TCC2**-*R*, perspective view [100]; (e) N_2 isotherms for **TCC1**-*R* (black squares), **TCC2**-*R* (blue triangles), **TCC3**-*R* (red diamonds), and **CC3**-*R* (green circles); adsorption = closed symbols, desorption = open symbols.

Figure 4. **Synthesis of 'isoreticular' racemic 1-D nanotubes.** (a) Single crystal structures of nanotubes formed by window-to-window packing of racemic **TCC1**, **TCC2**, and **TCC3** mixtures, as viewed perpendicular to the nanotubes and along a single nanotube pore channel. Solvent molecules and H atoms removed for clarity, simplified cyclohexyl vertices CHDA coloured red (-*R*) and turquoise (-*S*). (b, c) Offset, efficient crystal packing for racemic **TCC3** nanotubes (**TCC3**-*R* molecules coloured red, **TCC3**-*S* molecules coloured turquoise). (d, e) Space filling representation for racemic **TCC3** in 'closed', desolvated conformation (T = 350 K, d) and 'open', N_2-loaded conformation (T = 100 K, e), C, grey; N, blue; H omitted. (f, g) Plots showing visualization of pore size distribution for racemic **TCC3** in 'closed' (f) and 'open' conformations with associated crystal structures, C, grey; N, blue; H, white. (h) N_2 isotherms for racemic **TCC1** (black squares), **TCC2** (blue triangles), and **TCC3** (red diamonds); adsorption = closed symbols, desorption = open symbols.

Figure 5. **Predicted crystal energy landscapes.** Landscapes of predicted homochiral (a–c) and heterochiral crystal structures (d–f) for **TCC1** (a, d), **TCC2** (b, e) and **TCC3** (c, f). Each point corresponds to a distinct crystal structure. We show a 100 kJ mol^{-1} lattice energy range for all six landscapes. The wider landscape of **TCC3**-*R*/**TCC3**-*S* is shown in Supplementary Fig. 93. Green filled circles (a–c) and red filled circles (d–f) indicate predicted crystal structures that exhibit homochiral and heterochiral window-to-window packing, respectively. Predicted structures that match experimental structures are highlighted with cyan squares, showing their stability (in kJ mol^{-1}) relative to the global lattice energy minimum. No experimental crystallographic structure is available for **TCC3**-*R*, and no structural match could be found between the CSP dataset and experimental PXRD. Insets show overlays of 15-molecule clusters from the experimental (navy blue) and predicted (red) crystal structures. The best geometric overlay is given by the lowest root mean square deviation, RMSD, of atomic positions in the molecular cluster (Supplementary Fig. 96 for expanded images).

Figure 6. Reticular synthesis of pillared porous molecular networks by mixing linear ditopic cages and tetrahedral cages with opposing chirality. (a) Schematic representation of the desolvated single crystal structure, **TCC2**-*R*·(**CC3**-*S*)$_2$; intrinsic pore network shown in yellow. Pore size distribution plots for **TCC2**-*R*·(**CC3**-*S*)$_2$ showing (b) diamondoid intrinsic pore network (probe radii from 1.0 to 3.0 Å), and (c) extrinsic pore network between layers (probe radii from 3.0 to 6.0 Å). Colours are as in **Fig. 1e**; hydrogen atoms omitted for clarity. (d) Schematic representation of the desolvated single crystal structure of the 'isoreticular' analogue, **TCC1**-*R*·(**CC3**-*S*)$_2$, showing a reduced interlayer spacing.